Spin waves in the block checkerboard antiferromagnetic phase*

Lu Feng(卢 峰)† and Dai Xi(戴 希)

Beijing National Laboratory for Condensed Matter Physics, and Institute of Physics, Chinese Academy of Sciences, Beijing 100190, *China*

(Received 29 March 2011; revised manuscript received 27 October 2011)

Motivated by the discovery of a new family of 122 iron-based superconductors, we present the theoretical results on the ground state phase diagram, spin wave, and dynamic structure factor obtained from the extended J_1–J_2 Heisenberg model. In the reasonable physical parameter region of $K_2Fe_4Se_5$, we find that the block checkerboard antiferromagnetic order phase is stable. There are two acoustic spin wave branches and six optical spin wave branches in the block checkerboard antiferromagnetic phase, which have analytic expressions at the high-symmetry points. To further compare the experimental data on neutron scattering, we investigate the saddlepoint structure of the magnetic excitation spectrum and the inelastic neutron scattering pattern based on linear spin wave theory.

Keywords: spin wave, phase diagram, superconductivity

PACS: 75.30.Ds, 74.25.Dw, 74.20.Mn **DOI:** 10.1088/1674-1056/21/2/027502

1. Introduction

The search for a high-T_c superconductor has been one of the central topics in condensed matter physics.[1,2] Since the copper-based superconductor was discovered two decades ago,[3] a second class of high-transition temperature superconductor has been reported in iron-based pnictides.[4–7] The iron pnictide contains four typical crystal structures, such as 1111-type ReFeAsO (Re represents rare earth elements),[8] 122-type Ba(Ca)Fe_2As_2,[9,10] 111-type LiFeAs,[11] and 11-type FeSe.[12] The parent compounds with all structures, except for the 11-type, each have the stripe antiferromagnetic state as the ground state. By substituting a few percent of O with F[8] or Ba with K,[9,10] the compounds enter into the superconducting (SC) phase from the spin-density wave (SDW) phase below T_c. In addition to the above four crystal structures, a new family of iron-based superconducting materials with 122 types of crystal structures have recently been discovered with the transition temperature T_c as high as 33 K.[13–15] However, these new 122 compounds differ from the iron superconductors with other structures in many aspects.[16–20] Firstly, the parent compounds of the new 122 materials are proposed to be all $K_{0.8}Fe_{1.6}Se_2$ with intrinsic $\sqrt{5}\times\sqrt{5}$ Fe vacancy ordering determined by various experiments.[21–23] Secondly, the ground state for $K_{0.8}Fe_{1.6}Se_2$ is a Mott insulator with a block antiferromagnetic order (BAFM), which is observed by the neutron diffraction experiments.[21–23] By the first principles calculation, Yan *et al.*[24] and Cao and Dai[25] found that BAFM is the most stable ground state for $K_{0.8}Fe_{1.6}As_2$.

To date, a number of studies have been carried out to investigate the natures of superconductivity and magnetic properties of these materials.[26,27] The neutron scattering experiments[23] showed the ground state of $K_{0.8}Fe_{1.6}As_2$ to be BAFM with magnetic moment around 3.4 μ_B. It has been proposed by several authors that the magnetic and the superconducting instabilities are strongly coupled together and the properties of magnetic excitations, such as spin wave, play very crucial roles for the superconductivity in this family materials. Zhang *et al.*[28] even suggested that the superconducting pairing may be mediated by coherent spin wave excitations in these materials.

In order to give a qualitative insight into the magnetic excitation properties in this system, we study the spin wave spectrum using the Heisenberg model on a

*Project supported by the Science Foundation for Post-Doctorate Research from the Ministry of Science and Technology of China (Grant No. 20100470589), the National Basic Research Program of China (Grant No. 2007CB925000), and the National Natural Science Foundation of China (Grant No. 51071032).

†Corresponding author. E-mail: lufeng_china@126.com

© 2012 Chinese Physical Society and IOP Publishing Ltd

two-dimensional (2D) square lattice with $\sqrt{5}\times\sqrt{5}$ vacancy pattern. There are four independent parameters that are used in the model, which correspond to the nearest neighbour and the next nearest neighbour coupling between spins. We first obtain the ground state phase diagram as a function of those parameters, based on which we calculate the spin wave spectrum as well as the spin dynamic structure factor using the Holstein–Primakov transformation. Our results demonstrate that the block checkerboard antiferromagnetic order is stable in a wide range of phase regime and there are two acoustic spin wave branches and six optical spin wave branches in this system, which can be observed by neutron scattering experiments.

2. Model and method

The simplest model that captures the essential physics in Fe-vacancies ordered material $K_2Fe_4Se_5$ can be described by the extended J_1–J_2 Heisenberg model on a quasi-two-dimensional lattice as[24,25]

$$\begin{aligned} H = {} & J_1 \sum_{i,\delta,\delta'(>\delta)} \boldsymbol{S}_{i,\delta}\cdot\boldsymbol{S}_{i,\delta'} \\ & + J_1' \sum_{i,\gamma,\delta,\delta'} \boldsymbol{S}_{i,\delta}\cdot\boldsymbol{S}_{i+\gamma,\delta'} + J_2 \sum_{i,\delta,\delta''(>\delta)} \boldsymbol{S}_{i,\delta}\cdot\boldsymbol{S}_{i,\delta''} \\ & + J_2' \sum_{i,\gamma,\delta,\delta''} \boldsymbol{S}_{i,\delta}\cdot\boldsymbol{S}_{i+\gamma,\delta''}, \end{aligned} \tag{1}$$

where, $\delta = 1,2,3,4$ and $\gamma = 1,2,3,4$; the first and second terms represent the nearest-neighbour (NN) spin interactions in the intra- and the inter-blocks, as shown in Fig. 1. The third and fourth terms denote the next nearest-neighbour (NNN) spin interactions which are taken to be independent of the direction in the intra- and inter-blocks; i is the block index, γ denotes the nearest-neighbour block of the i-th block; $\delta'(\delta'')$ represents the site-index which is the NN (NNN) site of site δ. J_1 and J_1' (J_2 and J_2') indicate the NN (NNN) couplings of intra- and inter-blocks, respectively, which are illustrated in Fig. 1. Here, we define J_2 as the energy unit.

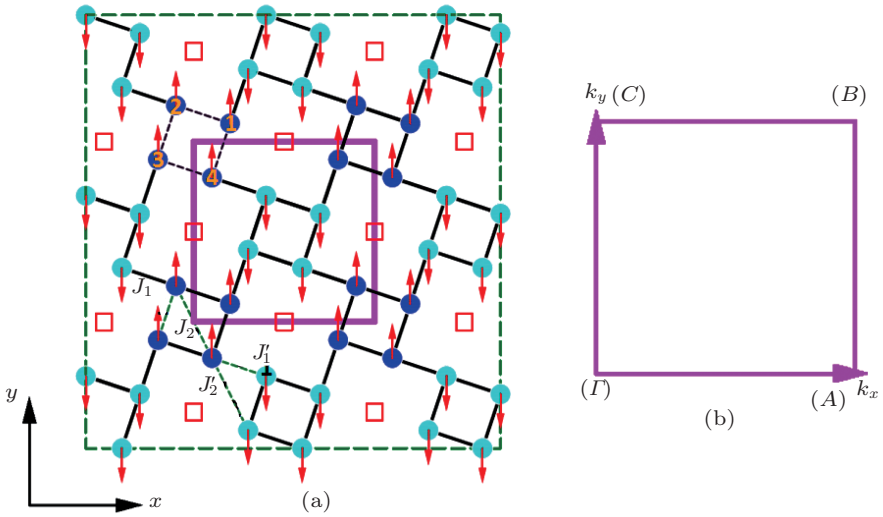


Fig. 1. (colour online) Schematic diagram of 2D and magnetic structure (single layer for $K_2Fe_4Se_5$) and the corresponding Brillouin zone. On the left (a) are the crystal structure and the spin pattern of the pnictides $K_2Fe_4Se_5$. The up-arrow (blue) and down-arrow (azure) atoms indicate the Fe-atoms with positive/negative magnetic moments, respectively. Here we show the considered model with the nearest neighbour couplings J_1, J_1' and the next nearest neighbour couplings J_2, J_2'. The coupling within each block is $J(J_1, J_2)$, and the coupling between blocks is $J'(J_1', J_2')$. On the right (b) is the positive quadrant of the square-lattice Brillouin zone with $\Gamma = (0,0)$, $A = (2\pi/\sqrt{10}a, 0)$, $B = (2\pi/\sqrt{10}a,\ 2\pi/\sqrt{10}a)$, and $C = (0, 2\pi/\sqrt{10}a)$. With the high symmetry line, the spin waves are contained along the direction $\Gamma - A - B - \Gamma - C - B$. The purple solid line denotes the magnetic unit cell. The iron vacancy site Fe is represented by the open square, and the occupied site Fe is marked by solid circle.

In order to understand this J_1–J_2 Heisengerg Hamiltonian, we depict the typical BAFM ground state and the two-dimensional (2D) Brillouin zone (BZ) in Fig. 1. Each magnetic unit cell contains eight Fe atoms and two Fe vacancies which are marked by the open squares. The BAFM was recently observed by the neutron diffraction experiment in the $K_2Fe_4Se_5$ material. An convenient way to understand the antiferromagnetic structure of $K_2Fe_4Se_5$ is to consider the four parallel magnetic moments in one block

as a supermoment; and the supermoments then form a simple chess-board nearest-neighbour antiferromagnetic order on a square lattice, as seen from Fig. 1(a). The distance between the nearest-neighbour irons is defined as a. Then, the crystal lattice constant for the magnetic unit cell is $\sqrt{10}a$. Figure 1(b) shows the 2D BZ for the magnetic unit cell. The q-vector used for defining the high symmetry line of the spin wave is also depicted.

We use a Holstein–Primakoff (HP) transformation to investigate the spin wave of BAFM ground state. As is well known, the linearized spin wave theory is a standard procedure to calculate the spin wave excitation spectrum and the zero-temperature dynamical structure factor.[29−31] Firstly, we use HP bosons to replace the spin operators, as shown in Appendix A. Using Holstein–Primakoff transformation, we can obtain the HP boson Hamiltonian as

$$H = \sum_k \psi_k^\dagger \mathscr{H}_k \psi_k + E_0 - N \cdot E_{(k=0)}, \qquad (2)$$

where,

$$\psi_k^\dagger = (a_{k1}^\dagger \ a_{k2}^\dagger \ a_{k3}^\dagger \ a_{k4}^\dagger \ b_{-k-1} \ b_{-k-2} \ b_{-k-3} \ b_{-k-4});$$

E_0 is the classical ground state energy for BAFM, $E_0 = 8J_1NS^2 - 4J_1'NS^2 + 4J_2NS^2 - 8J_2'NS^2$. The specific expression for $\mathscr{H}_k$ is shown in Appendix B.

In the real space, we define the 'molecular orbital', which is the combination of HP boson operators in one block as

$$\begin{aligned}
\alpha_{i1} &= \frac{1}{\sqrt{4}}(a_{i1} - a_{i2} + a_{i3} - a_{i4}), \\
\alpha_{i2} &= \frac{1}{\sqrt{4}}(a_{i1} + a_{i2} - a_{i3} - a_{i4}), \\
\alpha_{i3} &= \frac{1}{\sqrt{4}}(a_{i1} - a_{i2} - a_{i3} + a_{i4}), \\
\alpha_{i4} &= \frac{1}{\sqrt{4}}(a_{i1} + a_{i2} + a_{i3} + a_{i4}), \\
\beta_{i-1} &= \frac{1}{\sqrt{4}}(b_{i-1} - b_{i-2} + b_{i-3} - b_{i-4}), \\
\beta_{i-2} &= \frac{1}{\sqrt{4}}(b_{i-1} + b_{i-2} - b_{i-3} - b_{i-4}), \\
\beta_{i-3} &= \frac{1}{\sqrt{4}}(b_{i-1} - b_{i-2} - b_{i-3} + b_{i-4}), \\
\beta_{i-4} &= \frac{1}{\sqrt{4}}(b_{i-1} + b_{i-2} + b_{i-3} + b_{i-4}).
\end{aligned}$$

Here, the sign "–" represents the spin-down block. The corresponding physical picture for each 'molecular orbital' is shown in Fig. 2.

In the 'molecular orbital' basis, the Hamiltonian becomes

$$H_k = \sum_k \psi_k^{o\dagger} \mathscr{H}_k^{\text{orbital}} \psi_k^o. \qquad (3)$$

Here,

$$\psi_k^{o\dagger} = \alpha_{k1}^\dagger \ \alpha_{k2}^\dagger \ \alpha_{k3}^\dagger \ \alpha_{k4}^\dagger \ \beta_{-k-1} \ \beta_{-k-2} \ \beta_{-k-3} \ \beta_{-k-4}).$$

The matrix elements for different 'molecular orbitals' in the same block is zero, which is interesting; and we will discuss the Hamiltonian later. The specific expression for $\mathscr{H}_k^{\text{orbital}}$ is shown in Appendix B.

Because the boson Hamiltonian is big, one must use numerical diagonalization to solve eigenvalues for spin wave, which has a standard procedure[32−36] as shown in Appendix C.

To further understand the physical properties in this spin system, we obtain the analytical eigenvalues and eigenvectors at some special k points, such as $k = (0, 0)$ and $k = (\pi/\sqrt{10}a, \ \pi/\sqrt{10}a)$ points. At Γ point, the 'molecular orbitals' Hamiltonian becomes four 2×2 block matrixes $\begin{pmatrix} h_m & h_{m,m+4} \\ h_{m,m+4} & h_m \end{pmatrix}$ about α_m and $\beta_{-k-m}^\dagger$ $(m = 1, 2, 3, 4)$, which indicates that the 'molecular orbitals' are intrinsic vibration modes for Γ point. The spin waves at Γ point are induced by collective excitations of the same 'molecular orbitals' between different blocks.

From the 2×2 block Hamiltonian, we obtain the eigenvalues at Γ point as

$$\begin{aligned}
\omega_1^{(0,0)} &= S\sqrt{(4J_1 - J_1' - 2J_2')^2 - (J_1' - 2J_2')^2}, \\
\omega_2^{(0,0)} &= \omega_3^{(0,0)} \\
&= 2S\sqrt{(J_1 + J_2 - J_2')(J_1 - J_1' + J_2 - J_2')}, \\
\omega_4^{(0,0)} &= 0.
\end{aligned}$$

There are four eigenvalues. The first eigenvalue is twofold degenerate, and its eigenvector is a combination by the first 'molecular orbitals' at the spin-up and the spin-down block sites as shown in Fig. 2(a). The second and third eigenvalues are degenerate and each of them is twofold-degenerate. Their eigenvectors are combination by the second and the third 'molecular orbitals' at the spin-up and the spin-down block sites as shown in Figs. 2(b) and 2(c), respectively. They are all optical branches due to the gap at Γ point. The final eigenvalue is also twofold-degenerate. However, different from the above optical branches, the acoustic

branch is always zero at Γ point, which is imposed by Goldstone's theorem.

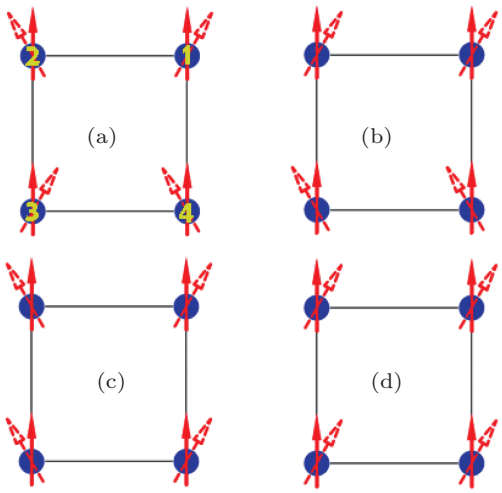


Fig. 2. (colour online) Schematic diagram for the 'molecular orbital' at the Γ point. (a) The deviations of spin orientations at sites 1 and 3 have the same phases for the corresponding wave function; and the deviations of spin orientations at sites 2 and 4 have the same phases for the corresponding wave function. However, the difference in the phase of wave function between sites 1 and 2 is 180°. (b) The deviations of spin orientations at sites 1 and 2 have the same phases for the corresponding wave function; and the deviations of spin orientations at sites 3 and 4 have the same phases for the corresponding wave function. However, the difference in the phase of the wave function between sites 1 and 3 is 180°. (c) The deviations of spin orientations at sites 1 and 4 have the same phases for the corresponding wave function; and the deviations of spin orientations at sites 2 and 3 have the same phases for the corresponding wave function. However, the difference in the phase of wave function between sites 1 and 2 is 180°. (d) The deviations of spin orientations at sites 1, 2, 3, and 4 all have the same phases for the corresponding wave function.

As shown above, we can also discuss the physical properties at $k = (\pi/\sqrt{10}a,\ \pi/\sqrt{10}a)$ point. From the boson Hamiltonian, we can obtain the eigenvalues at $k = (\pi/\sqrt{10}a,\ \pi/\sqrt{10}a)$ point as

$$\begin{aligned}
\omega_1^{(\pi,\pi)} &= -2SJ_1 + S\sqrt{(2J_1 - J_1' - 2J_2')^2 - {J_1'}^2}, \\
\omega_2^{(\pi,\pi)} &= 2SJ_1 + S\sqrt{(2J_1 - J_1' - 2J_2')^2 - {J_1'}^2}, \\
\omega_3^{(\pi,\pi)} &= \omega_4^{(\pi,\pi)} \\
&= S\sqrt{(2J_1 - J_1' + 2J_2 - 2J_2')^2 - 4{J_2'}^2 - {J_1'}^2}.
\end{aligned}$$

There are also four eigenvalues and each of them is twofold-degenerate. Six eigenvalues are for optical branches and two eigenvalues are for acoustic branches. The third and fourth eigenvalues are always degenerate at $k = (\pi/\sqrt{10}a,\ \pi/\sqrt{10}a)$ point.

Now, we have five different eigenvalues for the spin wave at the special point, which can be used to fit the experimental data in order to obtain the NN (NNN) couplings of intra- and inter-blocks, J_1, J_1' (J_2, J_2'). Then using this interaction parameters, we can obtain the spin wave along all the BZ by numerical diagonalization method.

3. Results and discussion

In this section, we first present the phase diagram of the J_1–J_2 model. Then we discuss the spin wave and the spin dynamical factor in the BAFM phase.

To investigate the phase diagram for the J_1–J_2 Heisenberg model, we use the stochastic Monte Carlo (MC) method to investigate the system ground state. In the reasonable physical parameter region, the phase diagram for the J_1–J_2 Heisenberg model is given in Fig. 3, which is plotted in the plane J_1/J_2–J_1'/J_2 at fixed value J_2'/J_2. We obtain four stable phases in the case $J_2'/J_2 = 1$. The first one is the block checkerboard antiferromagnetic order phase, denoted by AFM1 in Fig. 3, which has been observed in experiment.[21,22] This phase we are interested in is used to study the iron-based superconductors. Obviously, when the coupling J_1 is negative, the spin prefers to form ferromagnetic configuration in the block. Simultaneously, when the coupling J_1' is positive, the spin prefers to form antiferromagnetic configuration between the nearest-neighbour blocks. Of course, when J_1' is negative, but small, the interactions J_1 and J_2' are dominant and the block checkerboard antiferromagnetic phase is also stable in this region. In the case $J_2'/J_2 = 1$, the BAFM phase stably exists when the following conditions are satisfied: $J_1 < 0$ and $J_1' > J_1$. In the parameter region $J_1 > 0$ and $J_1 > J_1'$, the system prefers to stay in the AFM2 phase as seen in Fig. 3(a). In this phase, the antiferromagnetic order in the block arises from the antiferromagnetic coupling J_1. On the other hand, the spin system favours the AFM3 phase when $J_1' < J_1 < 0$, which is attributed mainly to the dominant interaction J_1' in this parameter region. Similar to the phase AFM3, the system stays in the AFM4 phase in the region $0 < J_1 < J_1'$ as seen in Fig. 3(a). To concretely investigate the spin properties in this system and compare the theoretical calculations with experimental results, we change the parameter value $J_2'/J_2 = 1$ to $J_2'/J_2 = 2.5$ to investigate the phase diagram. In this parameter re-

gion, the antiferromagnetic coupling J_2' is dominant. Unlike the first case, there are only two phase, AFM1 and AFM2, in the phase diagram. The two phases are separated by the line $J_1 = 0.5J_1'$. Below the line, the phase is AFM1 phase, and above the line, the phase is AFM2 phase. It is interesting to ask in which region the realistic parameters of the iron pnictides fall. From the local density approximation (LDA) calculations, Cao and Dai[19] suggested that $J_1 = -29$ meV, $J_1' = 10$ meV, $J_2 = 39$ meV, and $J_2' = 95$ meV. Such a set of parameters falls in the BAFM phase in Fig. 3(b), implying that the $K_2Fe_4Se_5$ should have the BAFM order. This fact implies that we only need to focus on parameter region in the AFM1 phase.

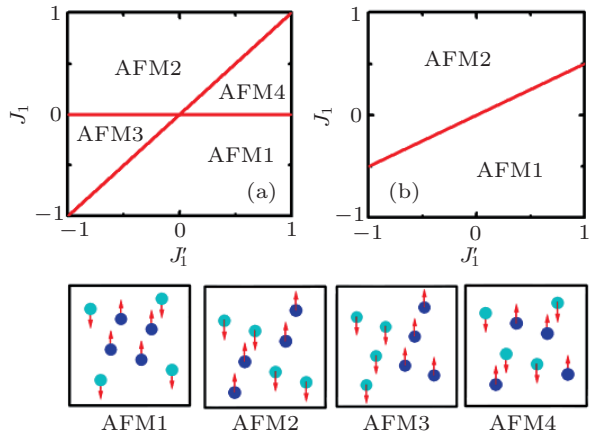


Fig. 3. (colour online) The phase diagram for the $J_1(J_1') - J_2(J_2')$ model. The AFM1 phase is the BAFM phase observed in the neutron diffraction experiment. The up-arrow (blue) and the down-arrow (azure) atoms indicate the Fe-atoms with positive/negative magnetic moments, respectively. The magnetic configurations for AFM2, AFM3, and AFM4 are also shown. Panel (a) shows the phase diagram for the interaction parameter $J_2 = 1, J_2' = J_2$, and panel (b) shows the phase diagram for the interaction parameter $J_2 = 1, J_2' = 2.5J_2$.

First of all, we use numerical diagonalization method to investigate the spin wave dispersion relations along the high symmetry direction in different cases. In the numerical calculation, it is convenient to set $J_2 = 1$; and by comparison with experimental results, the actual energy scale of J_2 for the specifical material can be deduced. Motivated by the first principles reported parameters,[25] we first study a set of parameters: (i) $J_1 = -1$, $J_1' = 0.2$, $J_2 = 1$, and $J_2' = 2.5$. However, to study the influence of interaction parameters on the spin-wave spectra, we also investigate four different sets of parameters: (ii) $J_1 = -1.5$, $J_1' = 0.2$, $J_2 = 1$, and $J_2' = 2.5$; (iii) $J_1 = -1$, $J_1' = 1.5$, $J_2 = 1$, and $J_2' = 2.5$; (iv) $J_1 = -1$, $J_1' = 0.2$, $J_2 = 0.2$, and $J_2' = 2.5$; (v) $J_1 = -1$, $J_1' = 0.2$, $J_2 = 1$, and $J_2' = 1.5$. In Fig. 4, we plot spin wave dispersions along high-symmetry direction $\Gamma - A - B - \Gamma - C - B$ in the BZ for different interaction parameters. In all the cases, there are one acoustic branch and three optical spin-wave branches (each of them is twofold-degenerate). For the acoustic branches, the gap of spin wave at Γ point is always zero due to Goldstone's theorem. In the first case, the vibration mode for acoustic branch is shown in Fig. 2(d). It is the collective excitation mode for the forward 'molecular orbitals' in one block with the forward 'molecular orbitals' in other blocks. The relative phase in a 'molecular orbital' is dependent only on the momentum k and independent of the interaction parameters. However, the relative phase between 'molecular orbitals' of different blocks is dependent on the specific interaction parameters. The optical gap at Γ point is dependent on the specific interaction parameters by contraries. As discussed in Eq. (4), two of the three optical branches are degenerate at Γ point. Away from Γ point, the two degenerate optical branches split. For example, with the increase of k along the Γ–B direction, the optical spin wave branch for the second 'molecular orbitals' (Fig. 2(b)) has almost no change. In contrast, the optical branch for the vibration mode of the third 'molecular orbitals' (Fig. 2(c)) has obvious dispersion, which can be clearly seen in Fig. 4(a). The reason for the splitting of spin wave can be attributed to the fact that the vibration modes of different 'molecular orbitals' are not isotropic and dependent on momentum k. Therefore, different vibration modes have different behaviours in different momentum directions. Similar to the above two optical branches, the third optical branch is related to the vibration mode of the first 'molecular orbitals', which is an independent branch.

With the change of interaction parameters, we can investigate the influence of the interaction parameters on the spin wave as shown in Fig. 4. Firstly, in all the cases, the acoustic branch is always zero at Γ point, and there are always twofold degenerate sites, i.e. points Γ and $k = (\pi/\sqrt{10}a,\ \pi/\sqrt{10}a)$. In the following, we compare the spin wave dispersion relations by changing interaction parameters. Comparing Fig. 4(a) with Fig. 4(b), we find that with the increase of J_1, the spin wave dispersions become bigger at different k points, especially for the acoustic branch at $k = (\pi/\sqrt{10}a,\ \pi/\sqrt{10}a)$ point. From Figs. 4(a) and

4(c), we observe that the amplitude of the second optical branch becomes large with the increase of J_1'. The energy for spin wave also changes with k point, especially at $k = (\pi/\sqrt{10}a,\ \pi/\sqrt{10}a)$ point. With the increase of J_1', the dispersion of the second optical branch becomes more and more clear. Comparing Figs. 4(a) and 4(d), we observe that the interval for the first and second optical branches becomes smaller with the increase of J_2. The energy for spin wave also changes with k point position, especially at the $k = (\pi/\sqrt{10}a,\ \pi/\sqrt{10}a)$ point. Like all the above cases, the spin wave dispersion also has some change in intensity with the increase of J_2'. However, the interval for the first and the second optical branches becomes larger, which is one of the most obvious features for increasing J_2' as seen in Figs. 4(a) and 4(e).

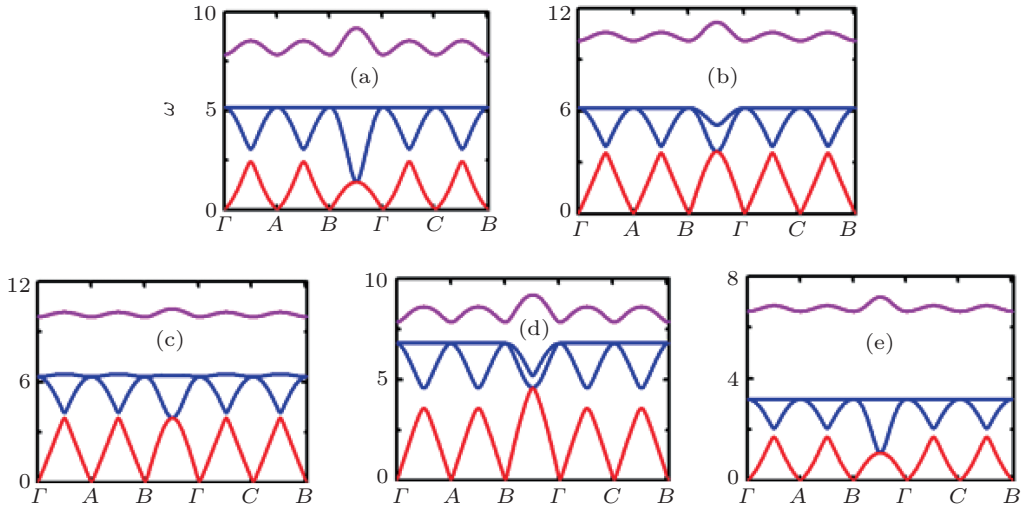


Fig. 4. (colour online) Acoustic and optical spin-wave branches for linear spin-wave theory each as a function of k along the selected high symmetry direction in the magnetic unit cell Brillouin zone. (a) $J_1 = -1$, $J_1' = 0.2$, $J_2 = 1$, and $J_2' = 2.5$, (b) $J_1 = -1.5$, $J_1' = 0.2$, $J_2 = 1$, and $J_2' = 2.5$, (c) $J_1 = -1$, $J_1' = 1.5$, $J_2 = 1$, and $J_2' = 2.5$, (d) $J_1 = -1$, $J_1' = 0.2$, $J_2 = 0.2$, and $J_2' = 2.5$, (e) $J_1 = -1$, $J_1' = 0.2$, $J_2 = 1$, and $J_2' = 1.5$. The x axis corresponds to the k point along the selected direction in Fig. 1(b). The y axis corresponds to the energy for spin wave; the energy is in units of J_2, i.e., $J_2 = 1$ except for the case (d).

Figure 5 shows the typical three-dimensional (3D) spin wave spectra in the extended BZ for one block of the first set of parameters in Fig. 4(a); and this plot provides a generally qualitative overview. Regardless of the specific parameter values, a common feature of the spin-wave dispersions is that there exist twofold degenerate sites, i.e., points Γ and $k = (\pi/\sqrt{10}a,\ \pi/\sqrt{10}a)$ and there is one zero branch at Γ point. One acoustic branch and three optical branches can also be seen, which is also a common feature in this system with the fixed saddlepoint structure. Generally speaking, we can determine the interaction parameters by comparing the spin-wave gaps at points Γ and $k = (\pi/\sqrt{10}a,\ \pi/\sqrt{10}a)$ with the experimental data; then we plot the spin wave using this set of parameters, which can be used to compare with the inelastic neutron scattering experiment.

As is well known, the neutron scattering cross section is proportional to the dynamic structure factor $S^{\rm in}(k,\omega)$. To further guide neutron scattering experiment, we plot the expected neutron scattering intensities at different constant frequency cuts in k-space. The zero-temperature dynamic structure factor can be calculated by Holstein–Primakoff bosons. In the linear spin wave approximation, S^z does not change the number of magnons, and only contributes to the elastic part of the neutron scattering intensity. However, $S^x(k)$ and $S^y(k)$ contribute to the inelastic neutron scattering intensity through single magnon excitations. The spin dynamical factor associated with the spin-waves is given by the expression as

$$S^{\rm in}(k,\omega) = S\sum_f \left|\langle f| \sum_{m=\pm\{1,2,3,4\}} \xi_{km}\alpha_m^\dagger|0\rangle\right|^2 \times \delta(\omega-\omega_f)\,. \quad (4)$$

Here $|0\rangle$ is the magnon vacuum state, $|f\rangle$ denotes the final state of the spin system with excitation energy, and ξ_{km} is the m-th component of the eigenvector $\alpha_m^\dagger|0\rangle$.[30,31]

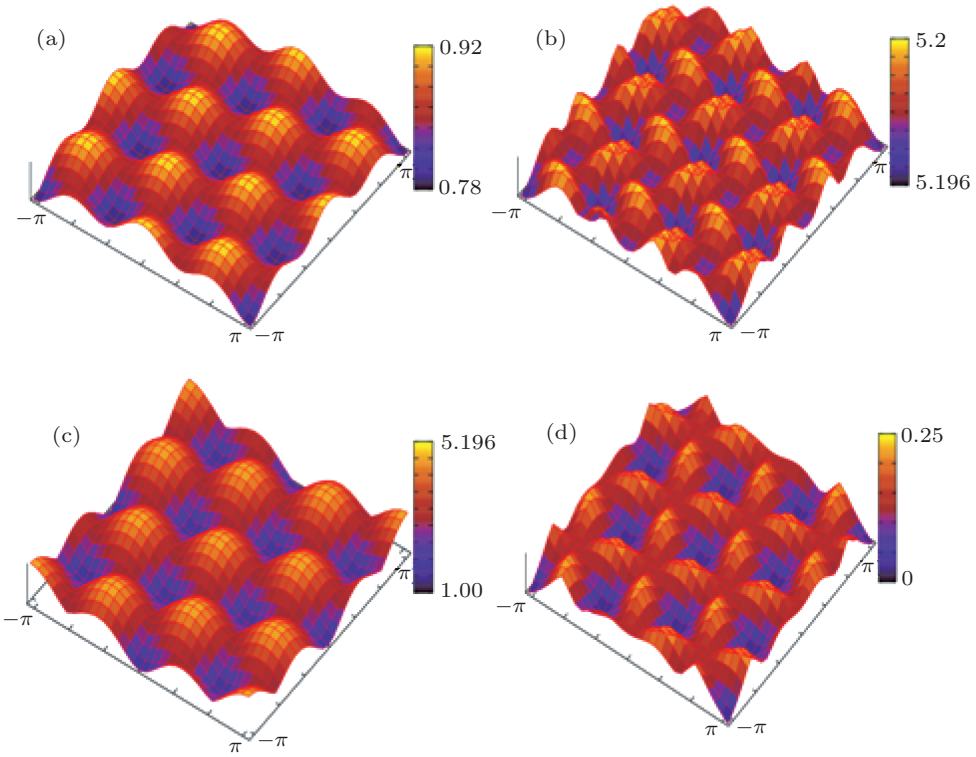


Fig. 5. (colour online) 3D spin wave dispersions for the parameter set of $J_1 = -1$, $J_1' = 0.2$, $J_2 = 1$, and $J_2' = 2.5$ in the extended BZ for one block as seen in Fig. 1(a). The energy is in units of J_2. (a) Spin wave dispersion for the first optical branch; (b) spin wave dispersion for the second optical branch; (c) spin wave dispersion for the third optical branch; (d) spin wave dispersion for acoustic branch. The x axis and y axis correspond to $3k_x - k_y$ and $k_x + 3k_y$ directions respectively.

Figure 6 shows our predictions for the intensity of the dynamical structure factor of the BAFM order (an untwinned case) each as a function of frequency. At low energy ($\omega = 0.5$), four strongest quadrate diffraction peaks are visible, which come from the acoustic spin-wave branch. With the increase of the cut frequency ($\omega = 1$), four strongest quadrate diffraction peaks disperse outward toward, which is also in the acoustic spin-wave branch range. At intermediate frequency ($\omega = 2$), the dynamic structure factor becomes a chain ring-shaped diffraction peaks, which is common results of the acoustic spin-wave branch and the first optical spin-wave branch. However, the intensity of diffraction peak around the Γ point is very weak. At high frequency ($\omega = 3.5$), the chain ring shape evolves into nine strong circle diffraction peaks, which come from the two optical spin-wave branches, which are degenerate at the Γ point. But the intensities of diffraction peaks around the Γ point are also very weak. Different from the low energy case at higher frequency ($\omega = 4.5$), the nine strong circle diffraction peaks do not disperse outward toward, but inward toward; simultaneously, the middle circle diffraction peak around the Γ point becomes weaker and vanishes with the increase of the frequency cut. The diffraction peak at this energy cut comes from the two optical spin-wave branches, which are degenerate at the Γ point. At highest frequency ($\omega = 9.0$), four strongest circle diffraction peaks are visible at the four corners of extended BZ and four weaker circle diffraction peaks are visible around the Γ point and the middle of the four boundaries, which come from the third optical spin-wave branch. The results are similar to those for other sets of parameters that have same ground states, with the main difference being that the energy cuts must be changed to obtain a similar spin dynamical factor patten.

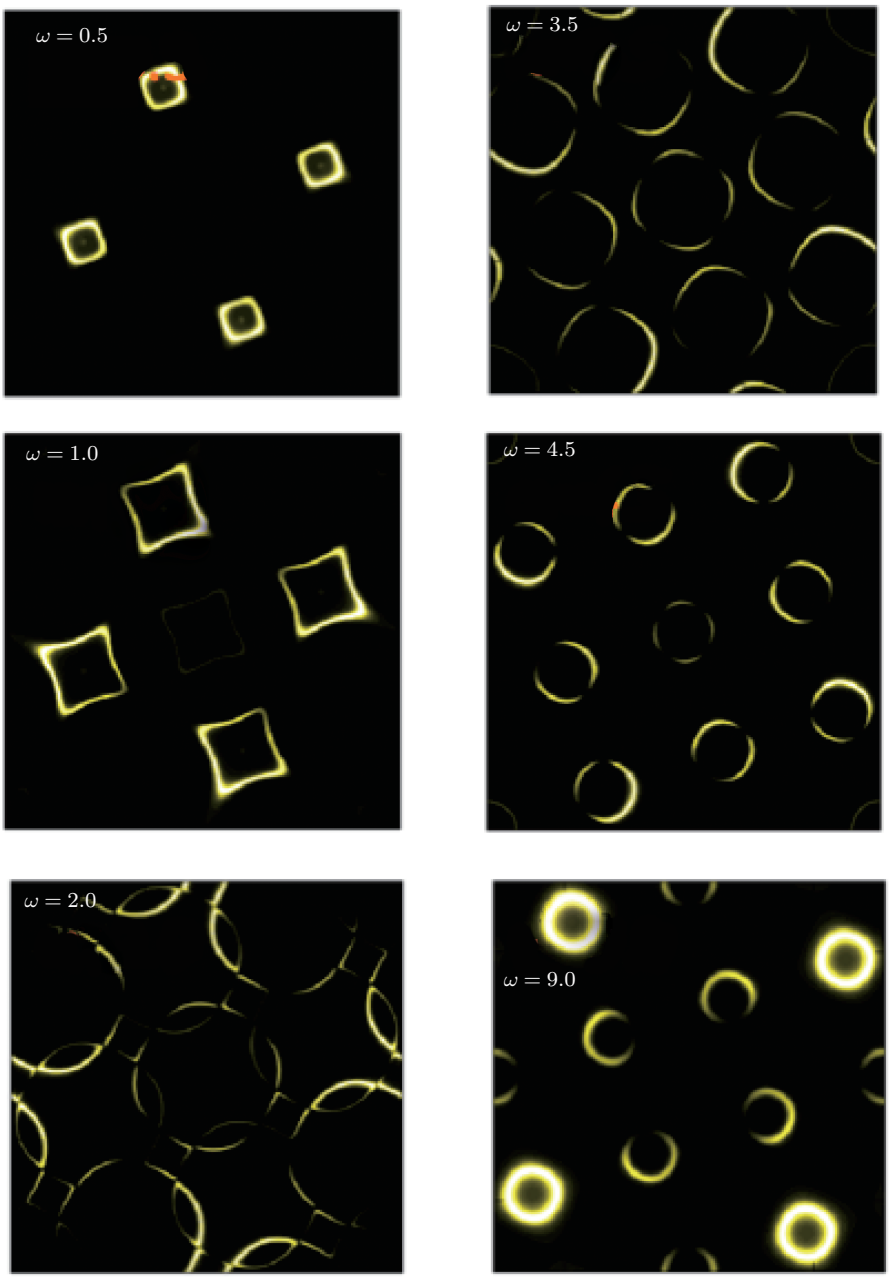


Fig. 6. (colour online) Constant-energy cuts (untwinned) of the dynamic structure factor $S^{\rm in}(k,\omega)$ for parameters: (i) $J_1 = -1$, $J_1' = 0.2$, $J_2 = 1$, and $J_2' = 2.5$, (ii) $J_1 = -1.5$ and the remaining parameters are the same as those in the case (i). The x axis and y axis correspond to $3k_x - k_y$ and $k_x + 3k_y$ directions in a range $(-\pi,\pi)$ respectively. The constant-energy cuts from top to down are $0.5J_2$, $1.0J_2$, $2.0J_2$, $3.5J_2$, $5.0J_2$, and $9.0J_2$ for all the energy ranges.

4. Discussion and conclusion

Using the J_1–J_2 Heisenberg model, we obtained the magnetic ground state phase diagram by using hte Monte Carlo approach and found that the BAFM order is stable in the reasonable physical parameter region of $K_2Fe_4Se_5$. We used the spin wave theory to investigate the spin wave and dynamic structure factor for the BAFM state. There are two acoustic branches and six optical branches of spin wave in this BAFM spin system, which are the combination of the 'molecular orbitals'. Then, we discussed the saddle-point structure in the magnetic excitation spectra, which can also be measured by neutron scattering experiments. The explicit analytical expressions for the spin-wave dispersion spectra at points Γ and $k = (\pi/\sqrt{10}a,\ \pi/\sqrt{10}a)$ are given. We also calculated the inelastic neutron scattering pattern to supply some references for future experimental studies. In addition, we also studied the specific influence

of each interaction parameter on the spin wave and dynamic structure factor. Neutron scattering experiments about the spin wave, especially the behaviour of spin wave in the proximity of a quantum critical point, deserve further attention.

Appendix A: Holstein–Primakoff transformation

The Holstein–Primakoff transformation is given as

$$\begin{aligned}\hat{S}_i^{\dagger} &= (\sqrt{2S - a_i^{\dagger}a_i})a_i \approx \sqrt{2S}a_i,\\ \hat{S}_i^{-} &= a_i^{\dagger}(\sqrt{2S - a_i^{\dagger}a_i}) \approx \sqrt{2S}a_i^{\dagger},\\ \hat{S}_i^{z} &= \left(S - a_i^{\dagger}a_i\right), \end{aligned} \tag{A1}$$

for $i = 1, 2, 3, 4$, which is occupied by spin-up; S represents the size of the magnetic moment for each iron; and

$$\begin{aligned}\hat{S}_{-i}^{\dagger} &= b_{-1}^{\dagger}(\sqrt{2S - b_{-i}^{\dagger}b_{-i}}) \approx \sqrt{2S}b_{-i}^{\dagger},\\ \hat{S}_{-i}^{-} &= (\sqrt{2S - b_{-i}^{\dagger}b_{-i}})b_{-i} \approx \sqrt{2S}b_{-i},\\ \hat{S}_{-i}^{z} &= \left(b_{-i}^{\dagger}b_{-i} - S\right), \end{aligned} \tag{A2}$$

for $i = 1, 2, 3, 4$, which is occupied by spin-down.

The Fourier transform for bosonic operators is

$$\begin{aligned} a_L &= N^{1/2}\sum_k \mathrm{e}^{\mathrm{i}\,k\cdot R_L}a_k, \quad a_L^{\dagger} = N^{1/2}\sum_k \mathrm{e}^{-ik\cdot R_L}a_k^{\dagger},\\ b_L &= N^{1/2}\sum_k \mathrm{e}^{\mathrm{i}\,k\cdot R_L}b_k,\\ b_L^{\dagger} &= N^{1/2}\sum_k \mathrm{e}^{-ik\cdot R_L}b_k^{\dagger}, \end{aligned} \tag{A3}$$

where N is the number of the magnetic unit cells, L the site index, and k the momentum index.

Appendix B: Spin wave Hamiltonian

We write the detailed expression in Eq. (2). Replacing the spin operators by Holstein–Primakoff (HP) boson operators, we can obtain the HP boson Hamiltonian $\mathscr{H}_k$ as

$$\begin{pmatrix} E_1 & F_k & G_k & S_k & 0 & (B_k)^* & (C_k)^* & (A_k)^*\\ (F_k)^* & E_1 & S_k & T_k & B_k & 0 & (A_k)^* & (D_k)^*\\ (G_k)^* & (S_k)^* & E_1 & (F_k)^* & C_k & A_k & 0 & B_k\\ (S_k)^* & (T_k)^* & F_k & E_1 & A_k & D_k & (B_k)^* & 0\\ 0 & (B_k)^* & (C_k)^* & (A_k)^* & E_1 & F_k & G_k & S_k\\ B_k & 0 & (A_k)^* & (D_k)^* & (F_k)^* & E_1 & S_k & T_k\\ C_k & A_k & 0 & B_k & (G_k)^* & (S_k)^* & E_1 & (F_k)^*\\ A_k & D_k & (B_k)^* & 0 & (S_k)^* & (T_k)^* & F_k & E_1 \end{pmatrix}, \tag{B1}$$

and

$$\begin{aligned} &E_k = J_1 + 1J_1' - 1J_2 + 2J_2', \quad A_k = J_2'S\,\mathrm{e}^{-\mathrm{i}\,\boldsymbol{k}\cdot\boldsymbol{x}_a}, \quad B_k = J_2'S\,\mathrm{e}^{\mathrm{i}\,\boldsymbol{k}\cdot\boldsymbol{y}_a}, \quad C_k = J_1'S\,\mathrm{e}^{-\mathrm{i}\,\boldsymbol{k}\cdot(0.5\boldsymbol{x}_a+0.5\boldsymbol{y}_a)},\\ &D_k = J_1'S\,\mathrm{e}^{\mathrm{i}\,\boldsymbol{k}\cdot(0.5\boldsymbol{x}_a-0.5\boldsymbol{y}_a)}, \quad F_k = SJ_1\,\mathrm{e}^{-\mathrm{i}\,\boldsymbol{k}\cdot(0.5\boldsymbol{x}_a-0.5\boldsymbol{y}_a)}, \quad G_k = SJ_2\,\mathrm{e}^{-\mathrm{i}\,\boldsymbol{k}\cdot\boldsymbol{x}_a}, \quad S_k = SJ_1\,\mathrm{e}^{-\mathrm{i}\,\boldsymbol{k}\cdot(0.5\boldsymbol{x}_a+0.5\boldsymbol{y}_a)},\\ &T_k = SJ_2\,\mathrm{e}^{-\mathrm{i}\,\boldsymbol{k}\cdot\boldsymbol{y}_a}, \quad \boldsymbol{x}_a = \sqrt{1.6}a\boldsymbol{i} + \sqrt{0.4}a\boldsymbol{j}, \quad \boldsymbol{y}_a = -\sqrt{0.4}a\boldsymbol{i} + \sqrt{1.6}a\boldsymbol{j}. \end{aligned}$$

In the 'molecular orbitals' basis, the Hamiltonian $\mathscr{H}_k^{\mathrm{orbital}}$ becomes

$$\frac{1}{4}\begin{pmatrix} E_o^1 & 0 & 0 & 0 & A_o & B_o & C_o & D_o\\ 0 & E_o^2 & 0 & 0 & (B_o)^* & F_o & -D_o & G_o\\ 0 & 0 & E_o^3 & 0 & (C_o)^* & -D_o & P_o & S_o\\ 0 & 0 & 0 & E_o^4 & D_o & (G_o)^* & (S_o)^* & T_o\\ A_o^4 & B_o & C_o & D_o & E_o^1 & 0 & 0 & 0\\ (B_o)^* & F_o & -D_o & G_o & 0 & E_o^2 & 0 & 0\\ (C_o)^* & -D_o & P_o & S_o & 0 & 0 & E_o^3 & 0\\ D_o & (G_o)^* & (S_o)^* & T_o & 0 & 0 & 0 & E_o^4 \end{pmatrix},$$

and

$$
\begin{aligned}
E_o^1 &= -16J_1 + 4J_1' + 8J_2', \\
E_o^2 &= -8J_1 + 4J_1' - 8J_2 + 8J_2', \\
E_o^3 &= -8J_1 + 4J_1' - 8J_2 + 8J_2', \\
E_o^4 &= 4J_1' + 8J_2', \\
A_o &= [2J_1' - 4J_2'][\cos(a_o) + \cos(b_o)], \\
B_o &= -2J_1'[\sin(a_o) + \sin(b_o)]\,\mathrm{i} + 4J_2' \sin(b_o)\,\mathrm{i}, \\
C_o &= -2J_1'[\sin(a_o) - \sin(b_o)]\,\mathrm{i} + 4J_2' \sin(a_o)\,\mathrm{i}, \\
D_o &= 2J_1'[\cos(a_o) - \cos(b_o)], \\
F_o &= -2J_1'[\cos(a_o) + \cos(b_o)] \\
&\quad - 4J_2'[\cos(a_o) - \cos(b_o)], \\
G_o &= 2J_1'[\sin(a_o) - \sin(b_o)]\,\mathrm{i} + 4J_2' \sin(a_o)\,\mathrm{i}, \\
P_o &= 4J_2'[\cos(a_o) - \cos(b_o)]] - 2J_1'[\cos(a_o) + \cos(b_o), \\
S_o &= 4J_2' \sin(b_o)\,\mathrm{i} + 2J_1'[\sin(a_o) + \sin(b_o)]\,\mathrm{i}, \\
T_o &= [2J_1' + 4J_2'][\cos(a_o) + \cos(b_o)], \\
a_o &= 1.5\boldsymbol{k} \cdot \boldsymbol{x}_a + 0.5\boldsymbol{k} \cdot \boldsymbol{y}_a, \\
b_o &= 0.5\boldsymbol{k} \cdot \boldsymbol{x}_a - 1.5\boldsymbol{k} \cdot \boldsymbol{y}_a.
\end{aligned}
$$

The matrix elements for different 'molecular orbitals' in the same block are all zero.

Appendix C: Numerical diagonalization method

We can use the numerical method to diagonalize the boson pairing Hamiltonian. The matrix form for boson Hamiltonian is

$$
\psi^\dagger \hat{\mathscr{H}} \psi = \begin{pmatrix} a^\dagger, b \end{pmatrix} \begin{pmatrix} A & B \\ B & A \end{pmatrix} \begin{pmatrix} a \\ b^\dagger \end{pmatrix},
$$

where $\psi^\dagger = (a^\dagger, b) = (a_1^\dagger, a_2^\dagger, a_3^\dagger, a_4^\dagger, b_{-1}, b_{-2}, b_{-3}, b_{-4})$; each of A and B is a 4×4 matrix; a and b are both boson operators. The operators satisfy the commutation relation

$$
\left[\psi_i, \psi_j^\dagger\right] = \hat{I}_{-i,j},
$$

and

$$
\hat{I}_- = \begin{pmatrix} I & 0 \\ 0 & -I \end{pmatrix},
$$

where I is a 4×4 identity matrix.

The diagonalization problem amounts to finding a transformation T, which lets $\hat{T}^\dagger \hat{\mathscr{H}} \hat{T}$ become a diagonalization matrix Ω.

$$
\psi = \begin{pmatrix} a \\ b^\dagger \end{pmatrix} = \hat{T} \begin{pmatrix} \alpha \\ \beta^\dagger \end{pmatrix} = \hat{T}\varphi.
$$

Here, we require that α and β are also a set of boson operators and

$$
\varphi^\dagger = (\alpha^\dagger, \beta) = (\alpha_1^\dagger, \alpha_2^\dagger, \alpha_3^\dagger, \alpha_4^\dagger, \beta_{-1}, \beta_{-2}, \beta_{-3}, \beta_{-4}).
$$

Then,

$$
\left[\psi_i, \psi_j^\dagger\right] = \hat{I}_{-i,j} = \sum_{i',j'} T_{i,i'} I_{-i',j'} T^\dagger_{j',j},
$$

we have

$$
\hat{T}\hat{I}_-\hat{T}^\dagger = \hat{I}_-. \tag{C1}
$$

Since $\hat{I}_-^2 = I$, we know $I = (\hat{I}_-\hat{T})(\hat{I}_-\hat{T}^\dagger)$. Due to the fact that $(\hat{I}_-\hat{T})$ and $(\hat{I}_-\hat{T}^\dagger)$ are both inverses, thus $I = (\hat{I}_-\hat{T}^\dagger)(\hat{I}_-\hat{T})$ and $\hat{T}^\dagger\hat{I}_-\hat{T} = \hat{I}_-$.

Then we want the final form of $\hat{\mathscr{H}}$ to be diagonalized

$$
\begin{aligned}
\hat{\mathscr{H}} &= \begin{pmatrix} a^\dagger, b \end{pmatrix} \begin{pmatrix} A & B \\ B & A \end{pmatrix} \begin{pmatrix} a \\ b^\dagger \end{pmatrix} \\
&= \psi^\dagger \hat{\mathscr{H}} \psi \\
&= \varphi^\dagger \left\{ \hat{T}^\dagger \begin{pmatrix} A & B \\ B & A \end{pmatrix} \hat{T} \right\} \varphi \\
&= \begin{pmatrix} \alpha^\dagger, \beta \end{pmatrix} \left\{ \hat{T}^\dagger \begin{pmatrix} A & B \\ B & A \end{pmatrix} \hat{T} \right\} \begin{pmatrix} \alpha \\ \beta^\dagger \end{pmatrix} \\
&= \begin{pmatrix} \alpha^\dagger, \beta \end{pmatrix} \{\hat{\Omega}\} \begin{pmatrix} \alpha \\ \beta^\dagger \end{pmatrix} \\
&= \varphi^\dagger \hat{\Omega} \varphi \\
&= \sum_i^4 \omega_i \alpha^\dagger \alpha + \omega_{-i} \beta \beta^\dagger,
\end{aligned} \tag{C2}
$$

where $\hat{\Omega} = \mathrm{diag}(\omega_1, \ldots, \omega_4, \omega_{-1}, \ldots, \omega_{-4})$ represents a diagonalized matrix and the matrix elements for diagonalized matrix are $\omega_1, \ldots, \omega_4, \omega_{-1}, \ldots, \omega_{-4}$.

In other words, we want the expression $\hat{T}^\dagger \hat{\mathscr{H}} \hat{T} = \Omega$ and matrix $\hat{\Omega}$ to be a diagonalized matrix. We must solve the matrix $\hat{T}$.

Combining Eqs. (C1) and (C2), we have

$$
\begin{aligned}
&\hat{T}^\dagger \hat{\mathscr{H}} \hat{T} = \hat{\Omega}, \\
&\left[\hat{T}\hat{I}_-\right] \hat{T}^\dagger \hat{\mathscr{H}} \hat{T} = \left[\hat{T}\hat{I}_-\right] \hat{\Omega}, \\
&\left[\hat{T}\hat{I}_-\hat{T}^\dagger\right] \hat{\mathscr{H}} \hat{T} = \left[\hat{T}\hat{I}_-\right] \hat{\Omega}, \\
&\hat{I}_- \hat{\mathscr{H}} \hat{T} = \left[\hat{T}\hat{I}_-\right] \hat{\Omega},
\end{aligned}
$$

$$(\hat{I}_-\hat{\mathscr{H}})\hat{T} = \hat{T}\left[\hat{I}_-\hat{\Omega}\right],$$
$$(\hat{I}_-\hat{\mathscr{H}})\hat{T} = \hat{T}\left[\hat{\lambda}\right], \quad \text{(C3)}$$

where $\hat{\lambda} = [\hat{I}_-\hat{\Omega}] = \mathrm{diag}(\omega_1, \ldots, \omega_4, -\omega_{-1}, \ldots, -\omega_{-4})$ is a diagonalization matrix. In other words, if we want to obtain $\hat{T}^\dagger\hat{\mathscr{H}}\hat{T} = \hat{\Omega}$, we can solve the general Hamiltonian $(\hat{I}_-\hat{\mathscr{H}})\hat{T} = \hat{T}[\hat{\lambda}]$. van Hemmen's[33] strategy is that the canonical transformation $\hat{T}$ is fully determined by its $n(=8)$ columns $\{x_1, \ldots, x_1, x_{-1}, \ldots, x_{-4}\}$. We, therefore, reduce Eq. (C3) to an eigenvalue problem for these $n(=8)$ vectors x_i, $1 \leqq i \leqq 8$.

Then

$$\left(\hat{I}_-\hat{\mathscr{H}}\right)\chi = \lambda\chi,$$

where $\chi = x_i$, $1 \leqq i \leqq 8$, and $\lambda \in \{\omega_1, \omega_2, \omega_3, \omega_4, -\omega_{-1}, -\omega_{-2}, -\omega_{-3}, -\omega_{-4}\}$. So, to diagonalize the Hamiltonian is equivalent to solving a general eigenvalue problem.

If we define that a matrix $\hat{I}_y = \begin{pmatrix} 0 & I \\ I & 0 \end{pmatrix}$ and I is a 4×4 identity matrix, it is easy to proof

$$\hat{I}_-\hat{\mathscr{H}} = -\hat{I}_y^{-1}\hat{I}_-\hat{\mathscr{H}}\hat{I}_y.$$

We assume that there is an eigenvalue λ_i and eigenvector $\chi_i = \begin{pmatrix} \mu_{1-4} \\ \nu_{1-4} \end{pmatrix}$ for the general Hamiltonian, then

$$\hat{I}_-\hat{\mathscr{H}}\chi_i = \lambda_i\chi_i.$$

Thus the $\chi_i' = \hat{I}_y \cdot \chi_i = \begin{pmatrix} \nu_{1-4} \\ \mu_{1-4} \end{pmatrix}$ is also an eigenvector of $\hat{I}_-\hat{\mathscr{H}}$ and the corresponding eigenvalue is $\lambda' = -\lambda$:

$$\begin{aligned}
&\hat{I}_-\hat{\mathscr{H}}\chi_i = \lambda_i\chi_i, \\
&-\hat{I}_y^{-1}\hat{I}_-\hat{\mathscr{H}}\left[\hat{I}_y\chi_i\right] = \lambda_i\chi_i, \\
&\hat{I}_y\hat{I}_y^{-1}\hat{I}_-\hat{\mathscr{H}}\left[\hat{I}_y\chi_i\right] = -\hat{I}_y\lambda_i\chi_i, \\
&\hat{I}_-\hat{\mathscr{H}}\left[\hat{I}_y\chi_i\right] = -\lambda_i\hat{I}_y\chi_i, \\
&I_-\hat{\mathscr{H}}\chi_i' = -\lambda_i\chi_i', \\
&I_-\hat{\mathscr{H}}\chi_i' = \lambda_i'\chi_i'.
\end{aligned}$$

Therefore, the eigenvalues are in pairs. For convenience, we arrange the order of eigenvalues by the relative size of the value $\aleph_i = \mid \mu_i \mid^2 - \mid \nu_i \mid^2$, $(\aleph_1 > \cdots > \aleph_8)$; for the same $\aleph_i$, we arrange the order of eigenvalues by its relative size. If the eigenvalue λ_i for the corresponding eigenvector $\aleph_1 > \aleph_2 > \aleph_3 > \aleph_4$ is lower than zero, it represents the unstable ground state. For the first four eigenvectors, $\mid \mu_i \mid^2 - \mid \nu_i \mid^2 = 1$ $(i = 1, 2, 3, 4)$ and for the last four eigenvectors, $\mid \mu_i \mid^2 - \mid \nu_i \mid^2 = -1$ $(i = 5, 6, 7, 8)$.

References

[1] Lee P A, Nagaosa N and Wen X G 2006 *Rev. Mod. Phys.* **78** 17

[2] Ma L, Huang A Q and Li J 2011 *Chin. Phys.* B **20** 037104

[3] Bednorz J G and Muller K A 1986 *Z. Phys.* B **64** 189

[4] Kamihara Y, Watanabe T, Hirano M and Hosono H 2008 *J. Am. Chem. Soc.* **130** 3296

[5] Chen G F 2008 *Phys. Rev. Lett.* **101** 057007

[6] Lei H, Wang K F, Warren J B and Petrovic C 2011 *Phys. Rev. Lett.* **107** 137002

[7] Yang S, You W L, Gu S J and Lin H Q 2009 *Chin. Phys.* B **18** 2545

[8] Kondo T, Santander-Syro A F, Copie O, Liu C, Tillman M E, Mun E D, Schmalian J, Budko S L, Tanatar M A, Canfield P C and Kaminski A 2008 *Phys. Rev. Lett.* **101** 147003

[9] Wray L, Qian D, Hsieh D, Xia Y, Li L, Checkelsky J G, Pasupathy A, Gomes K K, Parker C V, Fedorov A V, Chen G F, Luo J L, Yazdani A, Ong N P, Wang N L and Hasan M Z 2008 *Phys. Rev.* B **78** 184508

[10] Xu G, Zhang H J, Dai X and Fang Z 2008 *Europys. Lett.* **84** 67015

[11] Borisenko S V, Zabolotnyy V B, Evtushinsky D V, Kim T K, Morozov I V, Yaresko A N, Kordyuk A A, Behr G, Vasiliev A, Follath R and Bhner B 2010 *Phys. Rev. Lett.* **105** 067002

[12] Khasanov R, Bendele M, Amato A, Conder K, Keller H, Klauss H H, Luetkens H and Pomjakushina E 2010 *Phys. Rev. Lett.* **104** 087004

[13] Guo J, Chen X J, Zhang C, Guo J G, Chen X L, Wu Q, Gu D C, Gao P W, Dai X, Yang L H, Mao H K, Sun L L and Zhao Z X 2011 *arXiv*: 1101.0092

[14] Kawasaki Y, Mizuguchi Y, Deguchi K, Watanabe T, Ozaki T, Tsuda S, Yamaguchi T, Takeya H and Takano Y 2011 *arXiv*: 1101.0896

[15] Ying J J, Wang X F, Luo X G, Li Z Y, Yan Y J, Zhang M, Wang A F, Cheng P, Ye G J, Xiang Z J, Liu R H and Chen X H 2011 *New J. Phys.* **13** 033008

[16] Krzton-Maziopa A, Shermadini Z, Pomjakushina E, Pomjakushin V, Bendele M, Amato A, Khasanov R, Luetkens H and Conder K 2010 *J. Phys.: Condens. Matter* **23** 052203

[17] Ying J J, Wang X F, Luo X G, Wang A F, Zhang M, Yan Y J, Xiang Z J, Liu R H, Cheng P, Ye G J and Chen X H 2011 *Phys. Rev.* B **83** 212502

[18] Wang A F, Ying J J, Yan Y J, Liu R H, Luo X G, Li Z Y, Wang X F, Zhang M, Ye G J, Cheng P, Xiang Z J and Chen X H 2011 *Phys. Rev.* B **83** 060512

[19] Fang M H, Wang H D, Dong C H, Li Z J, Feng C M, Chen J and Yuan H Q 2011 *Europys. Lett.* **94** 27009

[20] Wang H D, Dong C H, Li Z J, Zhu S S, Mao Q H, Feng C M, Yuan H Q and Fang M H 2011 *Europys. Lett.* **93** 47004

[21] Bao W, Huang Q, Chen G F, Green M A, Wang D M, He J B, Wang X Q and Qiu Y 2011 *Chin. Phys. Lett.* **28** 086104
[22] Ye F, Chi S, Bao W, Wang X F, Ying J J, Chen X H, Wang H D, Dong C H and Fang M H 2011 *Phys. Rev. Lett.* **107** 137003
[23] Bao W, Li G N, Huang Q, Chen G F, He J B, Green M A, Qiu Y, Wang D M, Luo J L and Wu M M 2011 *arXiv*: 1102.3674
[24] Yan X W, Gao M, Lu Z Y and Xiang T 2011 *Phys. Rev.* B **83** 233205
[25] Cao C and Dai J 2011 *Phys. Rev. Lett.* **107** 056401
[26] You Y Z, Yao H and Lee D H 2011 *Phys. Rev.* B **84** 020406
[27] Fang C, Xu B, Dai P C, Xiang T and Hu J P 2011 *arXiv*: 1103.4599
[28] Zhang G M, Lu Z Y and Xiang T 2011 *Phys. Rev.* B **84** 052502
[29] Auerbach A 1994 *Phys. Rev. Lett.* **72** 2931
[30] Carlson E W, Yao D X and Campbell D K 2004 *Phys. Rev.* B **70** 064505
[31] Yao D X, Carlson E W and Campbell D K 2006 *Phys. Rev. Lett.* **97** 017003
[32] Xiao M W 2009 *arXiv*: 0908.0787
[33] Hemmen J L V 1980 *Z. Phys.* B **38** 271
[34] Lu H X and Zhang Y D 2000 *Int. J. Theor. Phys.* **39** 2
[35] Tsallis C 1978 *J. Math. Phys.* **19** 277
[36] Colpa J H P 1978 *Physica* A **93** 327